

# Iron Selenide Microcapsules as Universal Conversion-Typed Anodes for Alkali Metal-Ion Batteries

Shiyao Lu, Hu Wu, Siyuan Xu, Yuankun Wang, Jianyun Zhao, Yuhan Li, Amr M. Abdelkader, Jiao Li, Wei (Alex) Wang, Kai Xi,\* Yuzheng Guo, Shujiang Ding, Guoxin Gao,\* and Ramachandran Vasant Kumar

Rechargeable alkali metal-ion batteries (AMIBs) are receiving significant attention owing to their high energy density and low weight. The performance of AMIBs is highly dependent on the electrode materials. It is, therefore, quite crucial to explore suitable electrode materials that can fulfil the future requirements of AMIBs. Herein, a hierarchical hybrid yolk–shell structure of carbon-coated iron selenide microcapsules (FeSe<sub>2</sub>@C-3 MCs) is prepared via facile hydrothermal reaction, carbon-coating, HCl solution etching, and then selenization treatment. When used as the conversion-typed anode materials (CTAMs) for AMIBs, the yolk–shell FeSe<sub>2</sub>@C-3 MCs show advantages. First, the interconnected external carbon shell improves the mechanical strength of electrodes and accelerates ionic migration and electron transmission. Second, the internal electroactive FeSe<sub>2</sub> nanoparticles effectively decrease the extent of volume expansion and avoid pulverization when compared with micro-sized solid FeSe<sub>2</sub>. Third, the yolk–shell structure provides sufficient inner void to ensure electrolyte infiltration and mobilize the surface and near-surface reactions of electroactive FeSe<sub>2</sub> with alkali metal ions. Consequently, the designed yolk–shell FeSe<sub>2</sub>@C-3 MCs demonstrate enhanced electrochemical performance in lithium-ion batteries, sodium-ion batteries, and potassium-ion batteries with high specific capacities, long cyclic stability, and outstanding rate capability, presenting potential application as universal anodes for AMIBs.

## 1. Introduction

Rechargeable alkali metal-ion (such as Li<sup>+</sup>, Na<sup>+</sup>, and K<sup>+</sup>) batteries (AMIBs) are significant potential and practical energy storage devices.<sup>[1–3]</sup> As the most famous example, rechargeable lithium-ion batteries (LIBs) have dominated the market in portable electronics and electric vehicles over the past two decades.<sup>[4,5]</sup> However, the insufficient and uneven distribution of lithium resources raised concerns about the future deployment of LIBs.<sup>[6–8]</sup> Recently, many researchers have been focusing on exploring alternatives for LIBs. Sodium-ion batteries (SIBs) and potassium-ion batteries (PIBs) are considered as potential candidates due to the abundance and low cost of Na and K. Both SIBs and PIBs share a similar “rocking chair” energy storage mechanism with LIBs.<sup>[9–15]</sup> Unfortunately, considerable challenges remain in exploring the suitable electrode materials to host different alkali ions owing to the

S. Lu, H. Wu, Dr. Y. Wang, J. Zhao, Dr. Y. Li, J. Li, Prof. S. Ding, Dr. G. Gao  
Xi'an Key Laboratory of Sustainable Energy Materials Chemistry  
School of Chemistry  
Xi'an Jiaotong University & Shaanxi Quantong Joint Research  
Institute of New Energy Vehicles Power  
Xi'an Jiaotong University  
Xi'an 710049, China  
E-mail: gaoguoxin@mail.xjtu.edu.cn

S. Lu  
Department of Chemistry  
City University of Hong Kong  
Hong Kong 999077, China

 The ORCID identification number(s) for the author(s) of this article can be found under <https://doi.org/10.1002/smll.202005745>.

© 2021 The Authors. Small published by Wiley-VCH GmbH. This is an open access article under the terms of the Creative Commons Attribution-NonCommercial License, which permits use, distribution and reproduction in any medium, provided the original work is properly cited and is not used for commercial purposes.

DOI: 10.1002/smll.202005745

S. Xu, Prof. Y. Guo  
School of Electrical Engineering and Automation  
Wuhan University  
Wuhan 430072, China  
Prof. A. M. Abdelkader  
Faculty of Science and Technology  
Bournemouth University  
Talbot Campus, Fern Barrow, Poole BH12 5BB, UK

Prof. W. Wang  
Beijing Key Laboratory of Bio-inspired Energy Materials and Devices  
School of Space and Environment  
Beihang University  
Beijing 100191, China

Dr. K. Xi  
Cambridge Graphene Centre  
Department of Engineering  
University of Cambridge  
Cambridge CB3 0FA, UK  
E-mail: kx210@cam.ac.uk

Prof. R. V. Kumar  
Department of Materials Science and Metallurgy  
University of Cambridge  
Cambridge CB3 0FS, UK

increasing ionic radius and different interactions with the host electrodes.<sup>[16]</sup> In other words, except LIBs, other AMIBs are still in their infancy state with low capacities and problematic cyclic performance.

Conversion-typed anode materials (CTAMs) including transition metal oxides,<sup>[17]</sup> chalcogenides,<sup>[18–26]</sup> phosphides,<sup>[27–33]</sup> and nitrides<sup>[34,35]</sup> providing a promising prospect for AMIBs. The reactions on CTAMs are tunable and relying on the strong ionic bond between metal cations and the corresponding anions.<sup>[36–38]</sup> Compared with intercalation-typed (e.g., graphite) and alloy-typed (e.g., Sn/Sb) anode materials, CTAMs have higher theoretical capacity, more suitable volume variation, and lower production cost.<sup>[39–41]</sup> Additionally, CTAMs have been considered as the ideal candidate anodes for multiple alkali metal ions due to their similar reaction mechanisms and kinetic. However, the unstable structure and the continuous growth of solid electrolyte interphase (SEI) film on CTAMs are inevitable during the long-term discharge/charge cycling, thus causing fast capacity fading.<sup>[42,43]</sup> Mixing CTAMs with carbon nanomaterials and controlling the morphology of the electrodes have shown promising results on improving the structural stability of CTAMs, and consequently, boost the cycling lifespan with higher capacity at high current density.<sup>[39,42,44]</sup> However, addressing the problem of the contentious electrolyte decomposition due to some parasitic reactions, such as that responsible for SEI formation, remains a challenge. Approaches such as carbon coating and composite formations were reported to control the formation of the SEI layer but did not contribute much to enhance the structural stability of CTAMs. Hybrid carbonaceous yolk–shell structures, where CTAMs could occupy the core space and carbon acts as the shell, may represent an innovative solution to address both problems simultaneously. First, the carbon shell facilitates the formation of stable and robust SEI layer. Second, the preserved inner space within the hybrid yolk–shell structure maintains the structural integrity and alleviate the volume expansion during the electrode charging, which cannot be achieved by the traditional solid core–shell structures (Figure S1, Supporting Information).<sup>[27,45]</sup> Recently, a yolk–shell structure was applied in the construction of low-cost micro-structured anode materials, encouraging for further studies toward the industrial realization of CTAM-based batteries.<sup>[46]</sup> Therefore, it is logic to develop anodes for AMIBs that can take advantage of the synergy between yolk–shell structure and high energy density of CTAMs.

In this work, we choose yolk–shell FeSe<sub>2</sub> micro-sized capsules coated with amorphous carbon as the CTAMs for AMIBs. Our selection of FeSe<sub>2</sub> as the model active materials is based on their intrinsic semiconducting nature with rigid structure, high theoretical capacity and especially the outstanding ability to store various alkali metal ions.<sup>[47–49]</sup> The novel electrode (designated as carbon-coated iron selenide microcapsules (FeSe<sub>2</sub>@C-3 MCs) where “3” means the etching time of Fe<sub>3</sub>O<sub>4</sub>@C MCs intermediate templates is 3 h in the 3 M HCl solution) was synthesized via facial and easy to scale up process, giving a hierarchical porous structure with uniform distribution of the components. When used as CTAMs for AMIBs, the yolk–shell FeSe<sub>2</sub>@C-3 MCs demonstrate excellent electrochemical performance with high specific capacities, long cyclic stability, and outstanding rate capability benefiting from their highly enhanced structural stability and abundant near-surface

reactions, thus presenting potential application as universal anodes for AMIBs. Also, this synthesis route can be used to produce other micro-sized materials opening the door for more applications in the energy storage/conversion field.

## 2. Results and Discussion

Figure 1A schematically illustrates the fabrication procedure of the hierarchical hybrid yolk–shell FeSe<sub>2</sub>@C-3 MCs. First, Fe<sub>2</sub>O<sub>3</sub> micrometer ellipsoids (MEs) were prepared via a facile hydrothermal reaction as the initial templates. As shown in Figure S2B,C in the Supporting Information, the field-emission scanning electron microscopy (FESEM) images of as-prepared solid Fe<sub>2</sub>O<sub>3</sub> MEs reveal a highly uniform ellipsoid-like morphology with a length of ≈1.3 μm and width of ≈0.9 μm. The X-ray powder diffraction (XRD) pattern (Figure S2A, Supporting Information) proves that all the identified diffraction peaks belong to the hematite Fe<sub>2</sub>O<sub>3</sub> crystalline phase structure (JCPDS card no. 87-1165). Meanwhile, the energy dispersive X-ray (EDX) analysis (Figure S2D, Supporting Information) demonstrates that the atomic ratio of Fe and O elements is about 2:3 in the micro-ellipsoids, further confirming the successful formation of the hematite Fe<sub>2</sub>O<sub>3</sub> phase. Next, Fe<sub>2</sub>O<sub>3</sub> MEs are coated with polymeric resorcinol-formaldehyde (RF) layer, which further converts to amorphous carbon shell through thermal carbonization step at 500 °C in Ar/H<sub>2</sub> (9:1, volume ratio) atmosphere. This thermal treatment also reduces Fe<sub>2</sub>O<sub>3</sub> to Fe<sub>3</sub>O<sub>4</sub> and leads to the formation of carbon-coated Fe<sub>3</sub>O<sub>4</sub> (Fe<sub>3</sub>O<sub>4</sub>@C) MCs (Figure S3, Supporting Information). The XRD patterns and EDX spectroscopy confirmed that the reductive product is pure cubic Fe<sub>3</sub>O<sub>4</sub> phase (JCPDS card no. 75-0033). The atomic ratio of C, Fe, and O elements is calculated from the EDX analysis to be 4:7:9 (Figures S3D and S4, Supporting Information). The thickness of the carbon shell in the as-prepared core–shell Fe<sub>3</sub>O<sub>4</sub>@C MCs can be measured from the transmission electron microscopic (TEM) images (Figure S3C, Supporting Information) as ≈30 nm. Interestingly, after the thermal reduction, it can be found that several Fe<sub>3</sub>O<sub>4</sub>@C MCs are connected through their carbon shells, which is beneficial for electron transport. In the following step, the core–shell Fe<sub>3</sub>O<sub>4</sub>@C MCs are etched with 3 M HCl solution for 3 h to generate a large volume of void spaces between the internal Fe<sub>3</sub>O<sub>4</sub> core and external carbon shell. Thus, a hierarchical hybrid yolk–shell structure (Fe<sub>3</sub>O<sub>4</sub>@C-3 MCs) is formed (Figure S5, Supporting Information). In the final step, the Fe<sub>3</sub>O<sub>4</sub> is converted to FeSe<sub>2</sub> via thermal selenization. In the selenization process, Fe<sub>3</sub>O<sub>4</sub> reacts with Se vapor at 400 °C for 3 h using Ar/H<sub>2</sub> as the carrier gas, giving the final conformal structure FeSe<sub>2</sub>@C-3 MCs (Figure 1B–E). The XRD patterns of as-obtained selenization products confirm the complete conversion of cubic Fe<sub>3</sub>O<sub>4</sub> into orthorhombic FeSe<sub>2</sub> (JCPDS card no. 74-0247) (Figure 2A).<sup>[47]</sup> No other diffraction peaks can be detected from the XRD spectrum, suggesting the high purity of the yolk–shell FeSe<sub>2</sub>@C-3 MCs. The absence of any peaks related to carbon is due to the low crystallinity of the amorphous film. The TEM image of the yolk–shell FeSe<sub>2</sub>@C-3 MCs shown in Figure 1C revealed that FeSe<sub>2</sub> nanoparticles together and generate some void cavities. For comparison, the solid core–shell Fe<sub>3</sub>O<sub>4</sub>@C MCs without being

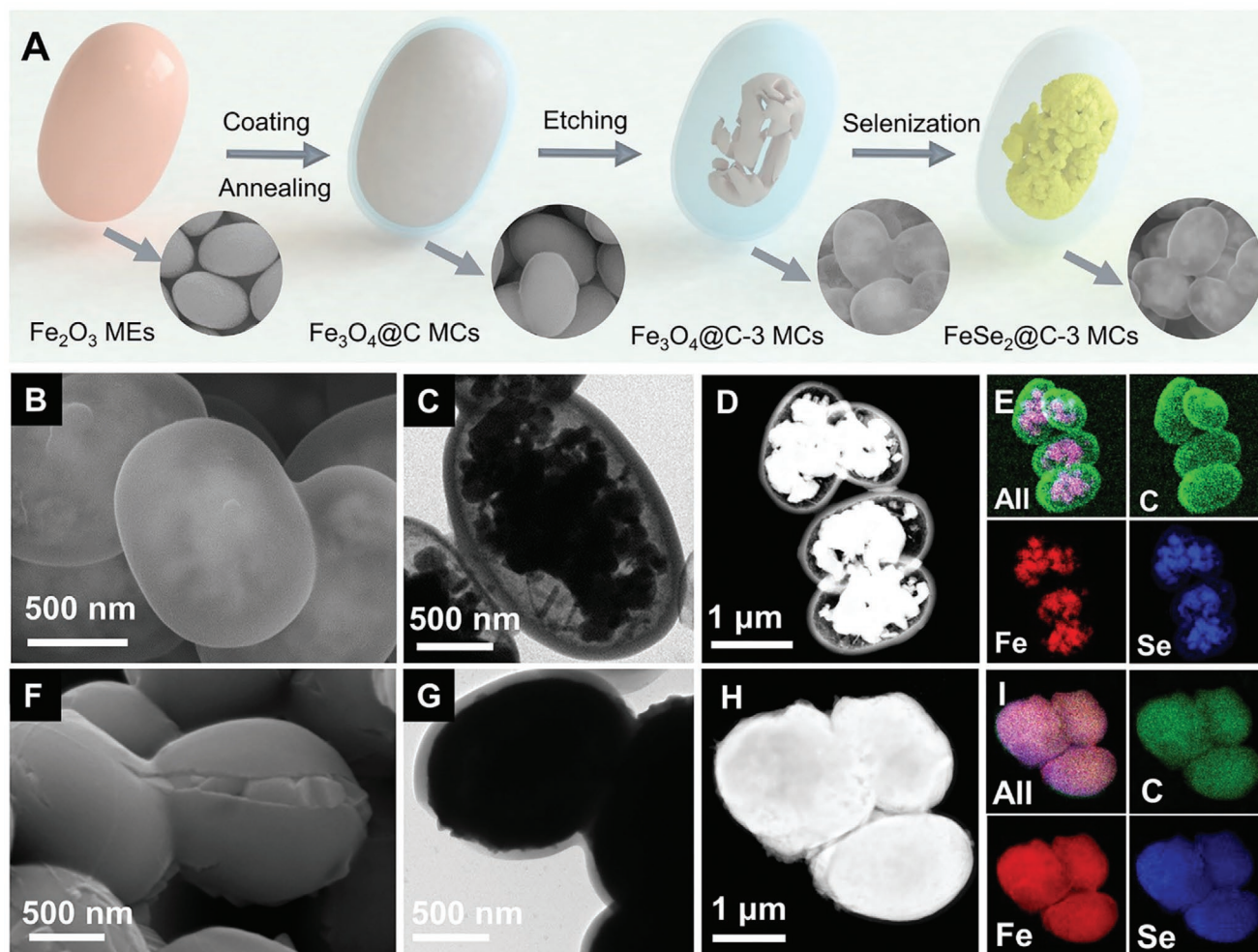


**Figure 1.** A) Schematic illustration of the synthetic process of yolk-shell  $\text{FeSe}_2@C-3$  MCs; B–I) FESEM, TEM, HAADF-STEM, and corresponding elemental mapping images of B–E) yolk-shell  $\text{FeSe}_2@C-3$  MCs and F–I) core-shell  $\text{FeSe}_2@C$  MCs.

etched by HCl solution are also annealed under the same selenization conditions but for a longer time (5 h) to complete the fully selenizing transformation (core-shell  $\text{FeSe}_2@C$  MCs). The XRD spectrum confirms the purity of the core-shell structure, without any secondary phases or contaminations. The interlayer distance, determined from the high-resolution transmission electron microscopic (HRTEM) image, is about 0.256 nm of the core-shell  $\text{FeSe}_2@C$  MCs, corresponding to the dominant (111) facet of  $\text{FeSe}_2$  (Figure S8, Supporting Information). High-angle annular dark-field (HAADF) scanning transmission electron microscopy (STEM) and the corresponding elemental mapping images of yolk-shell  $\text{FeSe}_2@C-3$  MCs and core-shell  $\text{FeSe}_2@C$  MCs also reveal the uniform distribution of Fe and Se elements within the hybrid structure. This demonstrates the successful diffusion of Se through the mesoporous carbon shell to react with Fe element and form the target hybrid (Figure 1D–E, H–I). However, yolk-shell  $\text{FeSe}_2@C-3$  MCs present hollow structure, while core-shell  $\text{FeSe}_2@C$  MCs give a solid structure. It can be seen from Figure 1F and Figure S6B in the Supporting Information that the selenization process has damaged the carbon shell in the nonetched samples, while that of the  $\text{FeSe}_2@C-3$

MCs with its hierarchical porous  $\text{FeSe}_2$  maintained a good shape without any noticeable damage (Figure 1B; Figure S6A, Supporting Information). Maintaining the structural integrity of the yolk-shell  $\text{FeSe}_2@C-3$  MCs after selenization is a good indicator that the void spaces within the structure can efficiently buffer the destructive effect of any phase transformation. It can also accommodate the volumetric expansion that might result from any similar process, such as the electrochemical charging.

Thermogravimetric analysis (TGA) was used to determine the thermal stability of the yolk-shell  $\text{FeSe}_2@C-3$  MCs and core-shell  $\text{FeSe}_2@C$  MCs. The slight weight increase between 200 and 312 °C can be attributed to the  $\text{FeSe}_2$  oxidation to  $\text{Fe}_2\text{O}_3$  and  $\text{SeO}_2$  (Figure 2B).<sup>[50]</sup> The dominant weight attenuation takes place between 400 and 500 °C is due to the volatilization of the newly formed  $\text{SeO}_2$  and the combustion of carbon shell according to the reaction:  $\text{FeSe}_2 + \text{C} + \text{O}_2 \rightarrow \text{Fe}_2\text{O}_3 + \text{SeO}_2\uparrow + \text{CO}_2\uparrow$ .<sup>[51]</sup> Therefore, the accurate carbon contents in the two samples are calculated to be 29.5 and 71 wt%, respectively. Raman spectra further confirm the existence of the carbonaceous component in both hybrids. As shown in Figure 2C, two characteristic D band ( $1377\text{ cm}^{-1}$ ) and G band ( $1589\text{ cm}^{-1}$ )

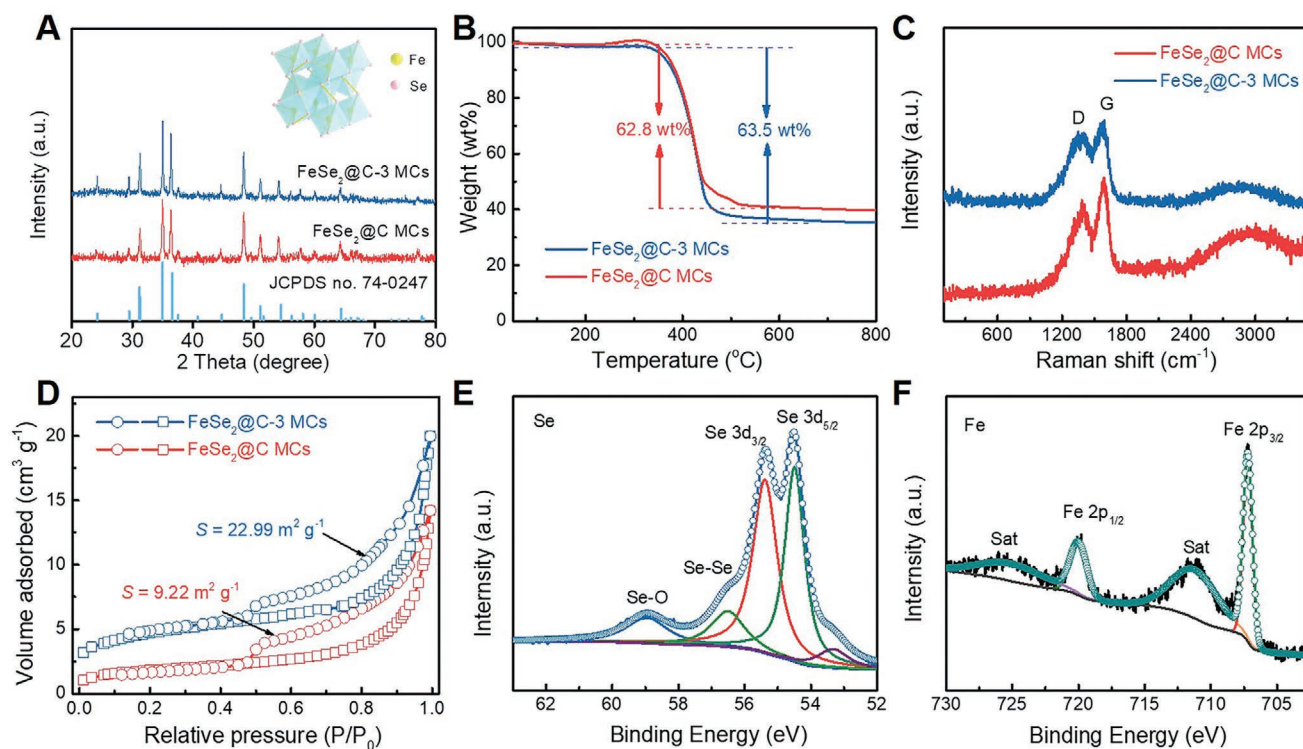


**Figure 2.** A) XRD spectra and crystal structure, B) TGA curves, C) Raman spectrum, and D) isotherm curves of adsorption–desorption of yolk–shell  $\text{FeSe}_2$ @C-3 MCs and core–shell  $\text{FeSe}_2$ @C MCs. E,F) High resolution XPS spectra of  $\text{FeSe}_2$ @C-3 MCs: E) Se 3d, F) Fe 2p.

are detected. The D band corresponds to the disordered carbon with structural defects, while G the band reveals the distinctive feature of graphitic carbon. The higher  $I_G/I_D$  ratio in the core–shell  $\text{FeSe}_2$ @C MCs can be ascribed to the longer calcination time, which leads to further graphitization of carbon in the composites. Additionally, the minor peak located at  $183.2\text{ cm}^{-1}$  on the Raman spectra is attributed to the Se–Se bonds of  $\text{FeSe}_2$ . The specific surface areas of core–shell  $\text{FeSe}_2$ @C MCs and yolk–shell  $\text{FeSe}_2$ @C-3 MCs are also measured using Brunauer–Emmert–Teller (BET) analysis. As presented in Figure 2D, the yolk–shell  $\text{FeSe}_2$ @C-3 MCs possess a larger specific surface area of  $23.0\text{ m}^2\text{ g}^{-1}$  than the core–shell  $\text{FeSe}_2$ @C MCs ( $9.22\text{ m}^2\text{ g}^{-1}$ ) due to the large volume of void spaces in the yolk–shell architecture. The X-ray photoelectron spectra (XPS) analysis was used to confirm the chemical valence states and bonds of  $\text{FeSe}_2$ @C-3 MCs. The high-resolution Se 3d spectrum in Figure 2E, shows three peaks at 54.5, 55.4, and 58.9 eV corresponding to the Se  $3d_{5/2}$  for the Fe–Se bonds, the Se  $3d_{3/2}$  for the Se–Se and Se–O bonds, respectively. Figure 2F exhibits the high-resolution Fe 2p spectrum. Apart from satellite peaks, there are two distinctive peaks at 707.2 and 720.0 eV, corresponding to Fe  $2p_{3/2}$  and Fe  $2p_{1/2}$  of iron selenide, respectively.<sup>[52]</sup> No sign of peaks corresponding to any Fe–O bonds, suggesting the carbon shell well protected the  $\text{FeSe}_2$  particles from atmospheric oxidation.

To evaluate the electrochemical performance of the yolk–shell  $\text{FeSe}_2$ @C-3 MCs, we first assembled coin-typed half-cells for lithium storage. Figure 3A presents the galvanostatic charge/discharge profiles of  $\text{FeSe}_2$ @C-3 MCs at a current density of  $0.5\text{ A g}^{-1}$ . After different cycles, the voltage plateaus change

gradually associated with increasing the specific capacity, indicating a typical activation process of metal selenides.<sup>[53]</sup> In cycling stability measurement, yolk–shell  $\text{FeSe}_2$ @C-3 MCs deliver a high reversible specific capacity of  $876.3\text{ mAh g}^{-1}$  with coulombic efficiency over 98% after 500 cycles, demonstrating high cyclic stability (Figure 3B). The  $\text{FeSe}_2$ @C-3 MCs electrode could undergo fast charge/discharge process and present excellent high-rate performance (Figure 3C). When cycled at higher current densities of 5 and  $10\text{ A g}^{-1}$ , the yolk–shell  $\text{FeSe}_2$ @C-3 MCs still delivered high capacities of 461.2 and  $311.2\text{ mAh g}^{-1}$ , respectively. We also summarize the lithium storage of recently reported  $\text{FeSe}_2$ -based anodes in Table S1 in the Supporting Information and conclude that our-designed yolk–shell  $\text{FeSe}_2$ @C-3 MCs outperforms other  $\text{FeSe}_2$  anodes in LIBs.

Inspired by the excellent lithium storage of our yolk–shell  $\text{FeSe}_2$ @C-3 MCs, we further measured their sodium and potassium storages. The assembled coin-typed half-cells of SIBs using ether-based electrolyte are cycled in the voltage window of 0.5–2.9 V. As shown in Figure 3D, a remarkable initial coulombic efficiency (ICE) of 92.8% can be achieved and maintained above 99.1% in the subsequent cycles. After the initial activation process, several stable voltage platforms are observed at 1.60, 1.08, and 0.75 V on the discharge curves, and 1.49 and 1.85 V on the charge curves. The long-term cyclic behavior of the yolk–shell  $\text{FeSe}_2$ @C-3 MCs was also estimated. As can be seen from Figure 3E, the discharge capacity of yolk–shell  $\text{FeSe}_2$ @C-3 MCs experience rapid initial rise, as in LIBs, to  $410\text{ mAh g}^{-1}$  within 40 cycles at  $1\text{ A g}^{-1}$  and then maintain a stable value over 1000 cycles. Even when cycled at a high current density of  $10\text{ A g}^{-1}$ , an impressive and stable reversible

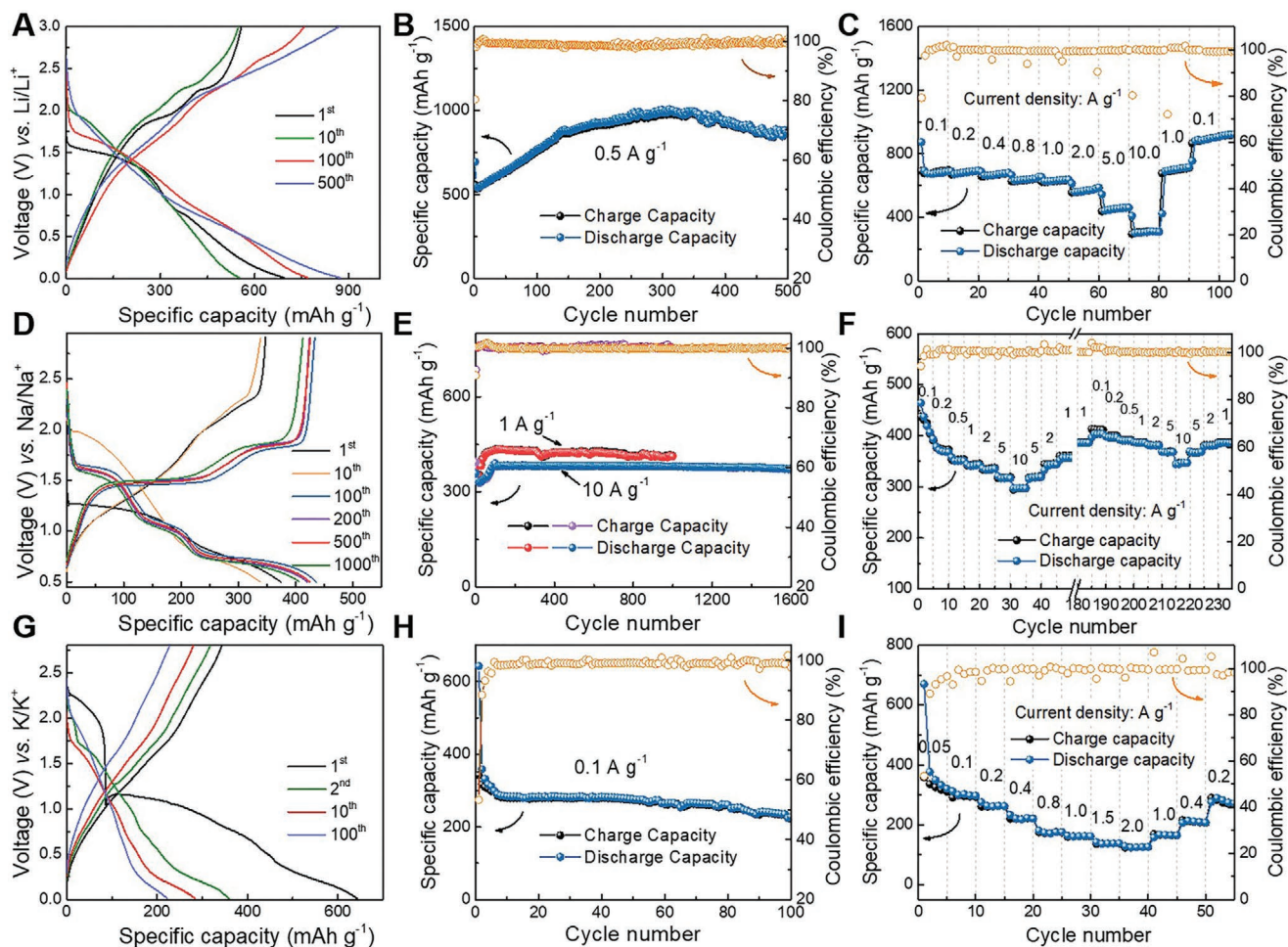


**Figure 3.** Electrochemical performances of FeSe<sub>2</sub>@C-3 MCs for A–C) LIBs, D–F) SIBs, and G–I) PIBs: A, D, G) Galvanostatic charge and discharge curves; B, E, H) Cycling stability and corresponding Coulombic efficiency at the designed current density; C, F, I) Rate capability under varying current densities.

discharge capacity of 371.7 mAh g<sup>-1</sup> could be maintained over 1500 cycles. The average capacity-fading per cycle is only 0.013%, indicating outstanding long-term cycle stability of the yolk-shell FeSe<sub>2</sub>@C-3 MCs for sodium storage. Figure 3F demonstrates the excellent high-rate performance of the yolk-shell FeSe<sub>2</sub>@C-3 MCs when cycled at different current densities between 0.1 and 10 A g<sup>-1</sup>. Remarkably, after the gradual activation under the current densities of 0.1 to 10 A g<sup>-1</sup> and continuously cycling at 1 A g<sup>-1</sup> for 185 cycles, the discharge capacity stabilizes at 403 mAh g<sup>-1</sup> for 0.1 A g<sup>-1</sup>, then slowly decreases to 347 mAh g<sup>-1</sup> with increasing the current density to 10 A g<sup>-1</sup>. The superior rate capability is evidenced from the immediate capacity recovery to 381 and 386 mAh g<sup>-1</sup> when the current densities return to 2 and 1 A g<sup>-1</sup>. This excellent electrochemical performance of the yolk-shell structure is outperforming or comparable with other FeSe<sub>2</sub> based anodes reported previously for SIBs (Table S2, Supporting Information).

We finally tested the potassium storage capacity of the yolk-shell FeSe<sub>2</sub>@C-3 MCs in a half-cell using coin-typed PIBs. As shown in Figure 3G, the yolk-shell FeSe<sub>2</sub>@C-3 MCs can deliver a high initial discharge capacity of 643.4 mAh g<sup>-1</sup> at a current density of 0.1 A g<sup>-1</sup>. The galvanostatic profiles are featureless after the first cycle, where only short voltage platforms

can be observed at 0.28 and 1.74 V in the charge and discharge profiles, respectively. A high discharge capacity of 2277 mAh g<sup>-1</sup> can be maintained after 100 cycles at 0.1 A g<sup>-1</sup> (Figure 3H). In addition, the continuous potassiation/depotassiation cycling process can still be conducted running at high rates. The discharge capacity decreases gradually from 376.8 to 141.8 mAh g<sup>-1</sup> as the current densities increasing from 0.05 to 2 A g<sup>-1</sup>, and finally stabilize at 289.9 mAh g<sup>-1</sup> when the current density turns back to 0.2 A g<sup>-1</sup> (Figure 3I), also presenting good rate performance.

To emphasize on the role of the internal voids on the electrochemical performance of the yolk-shell structure, we also measured the performance of the controlled core-shell FeSe<sub>2</sub>@C MCs (without HCl leaching) for all three AMIBs (Figure S9, Supporting Information). The specific capacities of the FeSe<sub>2</sub>@C MCs anode in LIBs and PIBs drop sharply upon cycling during the long-term cycle and high-rate measurements. For LIBs, the discharge capacity fails from ≈400 mAh g<sup>-1</sup> for the third cycle to below 200 mAh g<sup>-1</sup> after 120 cycles. The gradual increase of the capacity, which was attributed to the activation of the iron selenide in the case the yolk-shell anode, is not observed for FeSe<sub>2</sub>@C MCs, indicating the electrolyte is not able to access all the selenide due to the denser structure. For the PIBs, the initial discharge capacity recorded

for the  $\text{FeSe}_2/\text{C}$  MCs electrodes is  $\approx 410 \text{ mAh g}^{-1}$ , almost 50% less than the yolk-shell  $\text{FeSe}_2/\text{C}$ -3 MCs electrode. The discharge capacity decreases to around  $75 \text{ mAh g}^{-1}$  after 100 cycles, less than one-third of that recorded for the hierarchical yolk-shell anode. Although the assembled SIB using core-shell  $\text{FeSe}_2/\text{C}$  MCs as anode also demonstrates a gradual increase in the discharge capacity when cycled at  $1 \text{ A g}^{-1}$ , the reversible capacity drops to  $251 \text{ mAh g}^{-1}$  after 100 cycles. More importantly, when cycling at various current densities in the range  $0.1\text{--}10 \text{ A g}^{-1}$ , the rate performance in SIBs is extremely erratic, indicating its impracticality. All these results demonstrate the poor performance of the dense core-shell structure when compared with the well-engineered yolk-shell  $\text{FeSe}_2/\text{C}$ -3 MCs.

To investigate the electrochemical kinetics of the yolk-shell  $\text{FeSe}_2/\text{C}$ -3 MCs, CV profiles were recorded for LIBs, SIBs, and PIBs at various scan rates from  $0.2$  to  $1.5 \text{ mV s}^{-1}$  (Figure 4A–C). The CV curves show similar profiles to that reported in the literature for the Li, Na, K storage in  $\text{FeSe}_2$ -based anode.<sup>[53–55]</sup> In all the AMIBs, the CV curves display three reduction peaks and two oxidation peaks. In addition to the formation of the SEI layer in the first cycle, the three cathodic peaks can be attributed to the formation of various stoichiometries of the ternary

compound  $\text{M}_x\text{FeSe}_2$  (where M is Na, K, or Li). Peak 2 can be attributed to the formation of the more metallic phase FeSe and  $\text{M}_2\text{Se}$ . The last reduction peak (peak 3) can be attributed to the reduction of iron selenide to give Fe and  $\text{M}_2\text{Se}$ . During the anodic scans, two oxidation peaks can be observed; peak 4 for the back oxidation to form  $\text{M}_x\text{FeSe}_2$  and peak 5 for the formation of  $\text{FeSe}_2$ . For any redox peak, the relationship between the peak current and the scan rate can be used to give an idea about the reaction kinetics. Equation  $i = av^b$ , where ( $i$ ) is the peak current and ( $v$ ) the scan rate was used in the literature to determine if the current is a response of a slow diffusion process or a fast surface controlled process.<sup>[56,57]</sup> The  $b$ -value in these equation approaches to 1 for fast faradaic reactions on the exposed electrode surface, and to 0.5 for diffusion-controlled processes. For the  $\text{FeSe}_2/\text{C}$ -3 MCs electrode, the majority of the calculated  $b$  values for different current peaks approach to 1.0 in all the AMIBs systems (Figure 4D–F), indicating the electrochemical processes are dominated by surface-mediated capacitive behavior rather than an ionic diffusion-limited mechanism. To be more specific, the total capacitive behavior can be determined according to the equation:  $i = k_1v + k_2v^{0.5}$  ( $k_1v$ : capacitive behavior,  $k_2v^{0.5}$ : ionic diffusion behavior).<sup>[58]</sup>

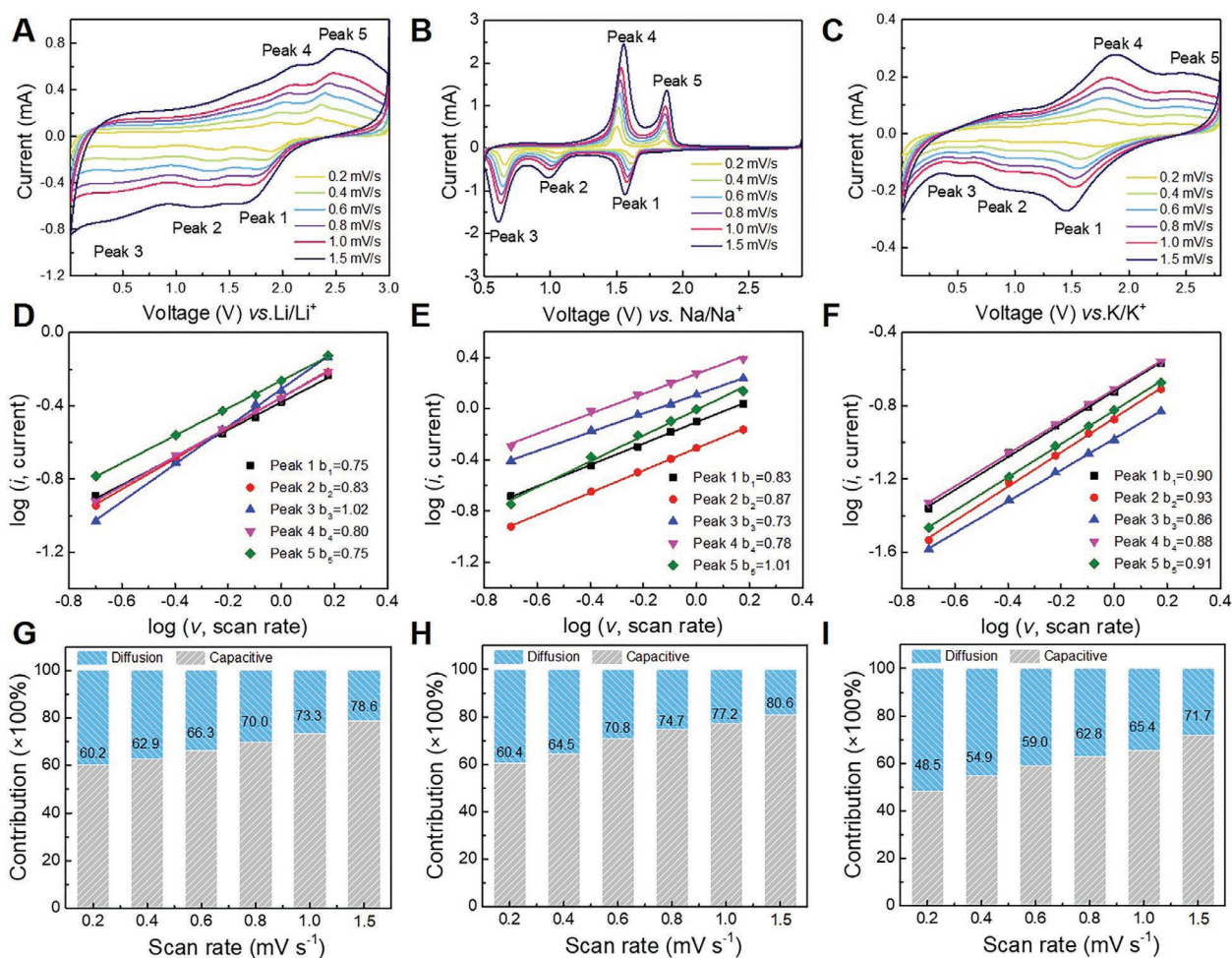


**Figure 4.** A–C) CV profiles, D–F) corresponding  $\log i$  versus  $\log v$  plot at each redox peak, and G–I) percent of pseudocapacitive contribution at different scan rates of  $\text{FeSe}_2/\text{C}$ -3 MCs in A,D,G) LIBs, B,E,H) SIBs, and C,F,I) PIBs storage.

As a result, we find that the capacitive behaviors of yolk-shell  $\text{FeSe}_2$ @C-3 MCs anodes increase gradually with the scan rates in the range from 0.2 to 1.5  $\text{mV s}^{-1}$ , (Figure 4G–I). For example, at 1  $\text{mV s}^{-1}$ , the capacitance proportions are 73.3%, 77.2%, and 65.4% when the yolk-shell  $\text{FeSe}_2$ @C-3 MCs electrode is used for LIBs, SIBs, and PIBs, respectively. These results demonstrate faster ion adsorption/desorption ability of the designed hierarchal yolk-shell anodes (Figure S10, Supporting Information). The electrochemical reaction dynamics of yolk-shell  $\text{FeSe}_2$ @C-3 MCs in the three kind AMIBs were further investigated by the galvanostatic intermittent titration technique (GITT) to calculate the ionic diffusion coefficient ( $D$ ). Figure S1 in the Supporting Information reveals the GITT curves and the corresponding  $\text{Li}^+$ ,  $\text{Na}^+$ , and  $\text{K}^+$  ions chemical diffusion coefficient of yolk-shell  $\text{FeSe}_2$ @C-3 MCs as a function of reaction depth. The  $D$  values calculated from the GITT profiles are in the range of  $10^{-12}$ – $10^{-9}$   $\text{cm}^2 \text{s}^{-1}$ , showing the effectiveness of the new design of the electrode on boosting the kinetics of the reaction. It should be noted here that the overpotential of yolk-shell  $\text{FeSe}_2$ @C-3 MCs for PIB is slightly higher than that for LIB and SIB, which could be related to its lower pseudocapacitive contribution and a larger radius of  $\text{K}^+$ .<sup>[59]</sup> Noticeably, the overpotential in the charging process is as low as 0.18 V, suggesting fast  $\text{K}^+$  diffusion in the depotassiation stage.

We further examined the possible electrochemical reaction mechanism of yolk-shell  $\text{FeSe}_2$ @C-3 MCs in PIBs using in situ XRD and ex situ XPS measurements. As shown in Figure 5A, the characteristic peaks of  $\text{FeSe}_2$  diminish gradually at the first stage of the discharge process without any other visible changes in the XRD spectra. Then, new peaks at  $30.4^\circ$  and  $28.5^\circ$  appear after passing 1.0 V, corresponding to the (040), (101) crystal planes of intermediate  $\text{KFeSe}_2$  and  $\text{FeSe}$ , respectively.<sup>[20]</sup> The peak at  $29.4^\circ$  is enhanced because of the formation of  $\text{KFeSe}_2$  ((22 $\bar{1}$ ) facet) overlapping with the peak of  $\text{FeSe}_2$  ((101) facet). The complete discharge products are relatively complicated. Both  $\text{K}_5\text{Se}_3$  and  $\text{K}_2\text{Se}_3$  phases could be detected and partially remain in the following charging process (Figure S12, Supporting Information).<sup>[60]</sup> When fully charged, the (101), (110), and (111) crystal facets of orthorhombic  $\text{FeSe}_2$  phase recovered again. At the same time, the  $\text{FeSe}$  and  $\text{KFeSe}_2$  phases also appear at intermediate stages of the charging, indicating a partially reversible conversion reaction mechanism. Figure 5B presents the high-resolution Se 3d XPS spectra at different discharge/charge stages. When discharged from 1.2 to 0.01 V the relative intensity of the Se  $3d_{3/2}$  peak at 54.9 eV increases gradually, while that of the Se  $3d_{5/2}$  peak at 54.1 eV decreases, which can be attributed to the formation of K–Se bond and the cleavage of Fe–Se bond, respectively.<sup>[61,62]</sup> After fully charged at 2.8 V, Se  $3d_{5/2}$  peak became

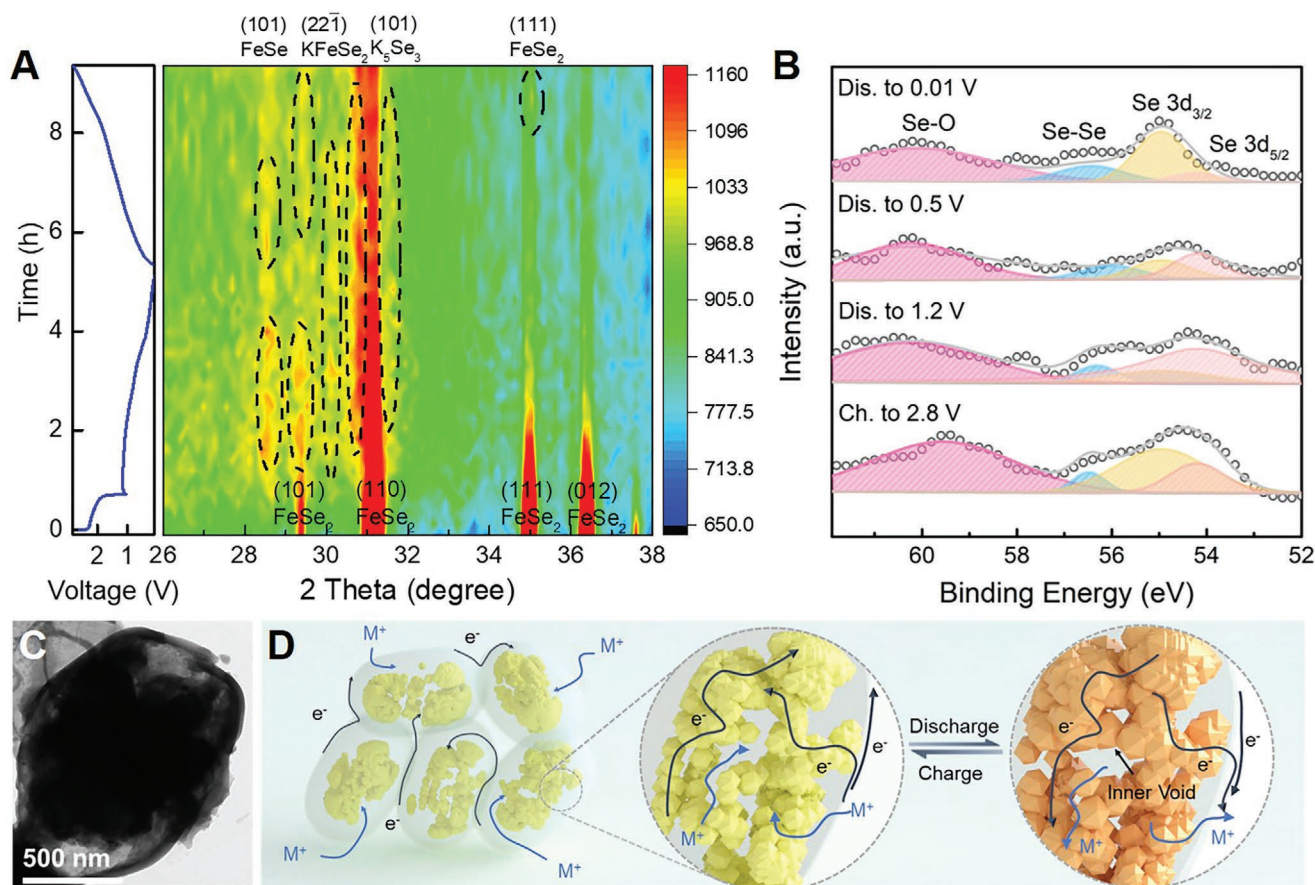


**Figure 5.** A) In situ XRD patterns of  $\text{FeSe}_2$ @C-3 MCs electrode in the first cycle in PIBs; B) Se 3d high-resolution XPS spectra of  $\text{FeSe}_2$ @C-3 MCs at various stages of the charging/discharging; C) Ex situ TEM image of  $\text{FeSe}_2$ @C-3 MCs after 100 cycles in PIBs; D) Schematic illustration of the reaction mechanism of  $\text{FeSe}_2$ @C-3 MCs in AMIBs.

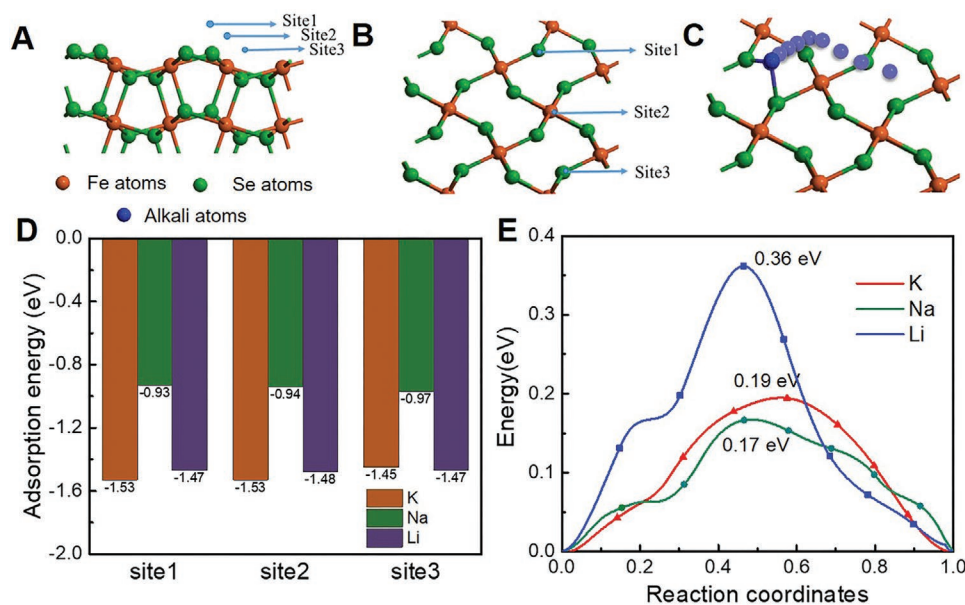


**Figure 6.** The adsorption sites A) side view, B) overview, and C) Diffusion process of Li, Na, and K atoms. D) Adsorption energy and E) diffusion energy of Li, Na, and K atoms.

more distinctive, confirming the reversible processes during consecutive potassiation/depotassiation. We have summarized all the possible reactions mechanisms in Table S4 in the Supporting Information, based on the above results.

Furthermore, the volume change and structural stability are evaluated by ex situ scanning electron microscopy (SEM) and TEM. As shown in Figure S13 in the Supporting Information, yolk-shell FeSe<sub>2</sub>@C-3 MCs still maintain their initial morphology after consecutive 100 cycles in the three storage systems. Figure 5C shows one representative TEM image, revealing that the initial void spaces are still maintained after long-term cycling in PIBs. The volume expansion/contraction and the ionic diffusion paths of the yolk-shell electrodes are schematically depicted in Figure 5D. Generally, both interconnected external carbon shell and internal FeSe<sub>2</sub> nanoparticles facilitate electronic conductivity. The electrochemical impedance spectra (EIS) of the fresh FeSe<sub>2</sub>@C-3 MCs electrode and after 100 cycles in the battery systems are presented in Figure S14 in the Supporting Information. Apparently, after 100 cycle tests, the semicircle radius of yolk-shell FeSe<sub>2</sub>@C-3 MCs in the high-frequency region is smaller than that of the controlled core-shell FeSe<sub>2</sub>@C MCs, especially for the PIBs, demonstrating higher electric conductivity and lower interfacial resistance after activation.

The ion diffusion behavior of alkali ions inside FeSe<sub>2</sub> was further investigated by density functional theory (DFT) calculations. As presented in Figure 6, all the three different alkali atoms reveal negative adsorption energy, indicating a good adsorption performance. For a certain alkali atom, all sites yield similar adsorption energy, suggesting that atoms move to the same place during the relaxation. After examining the final optimized image, site1 is chosen as the initial and final position in the diffusion process. Among all alkali atoms, K atom exhibits the lowest adsorption energy (−1.53 eV), further proving the potential of FeSe<sub>2</sub> in KIBs. In the diffusion process, the Na and K atoms show a relatively lower energy barrier, indicating an

easier diffusion process and higher rate capacity (Figure 6E). The combination of Na atoms and FeSe<sub>2</sub> material manifests the lowest diffusion energy, which is consistent with the good performance of SIBs revealed by the experimental results.<sup>[53]</sup>

In summary, yolk-shell FeSe<sub>2</sub>@C-3 MCs have been successfully fabricated by a facile solvothermal method, HCl etching, and selenization process. When used as typical CTAMs for AMIBs, it manifests excellent electrochemical performance. The well-designed yolk-shell structure can efficiently alleviate the volume expansion and promote electronic conductivity during consecutive Li<sup>+</sup>, Na<sup>+</sup>, and K<sup>+</sup> ions insertion. As a result, the yolk-shell FeSe<sub>2</sub>@C-3 MCs electrodes have achieved high reversible capacity, long-term cycle stability, and excellent high-rate performance in LIBs and SIBs. Besides, we also demonstrate the potential of such FeSe<sub>2</sub>-based anodes in PIBs. The reaction mechanism has been systematically disclosed by in/ex situ measurement and DFT calculation. Furthermore, our research paves the way to construct other micro-sized CTAMs for multiple metal ion battery systems.

## Supporting Information

Supporting Information is available from the Wiley Online Library or from the author.

## Acknowledgements

S.L., H.W., and S.X. contributed equally to this work. This research was supported by the National Natural Science Foundation of China (No. 51773165, 51973171), Natural Science Foundation of Shaanxi Province (No. 2019JM-175), Key Laboratory Construction Program of Xi'an Municipal Bureau of Science and Technology (201805056ZD7CG40). The Center for Advancing Materials Performance from the Nanoscale (CAMP-Nano) is acknowledged for allowing the use of field-emission scanning electron microscopy. Miss Jiao Li at Instrument Analysis Center of Xi'an Jiaotong University is thanked for her assistance with TEM Mapping measurement.

## Conflict of Interest

The authors declare no conflict of interest.

## Keywords

alkali metal-ion batteries, conversion reactions, iron selenides, yolk-shell structures

Received: September 15, 2020

Revised: November 12, 2020

Published online: January 31, 2021

- [1] E. Pomerantseva, F. Bonaccorso, X. Feng, Y. Cui, Y. Gogotsi, *Science* **2019**, 366, 969.
- [2] Y. Liu, Y. Zhu, Y. Cui, *Nat. Energy* **2019**, 4, 540.
- [3] T. Shao, C. Liu, W. Deng, C. Li, X. Wang, M. Xue, R. Li, *Batteries Supercaps* **2019**, 2, 403.
- [4] S. Fang, D. Bresser, S. Passerini, *Adv. Energy Mater.* **2020**, 10, 1902485.
- [5] J. W. Choi, D. Aurbach, *Nat. Rev. Mater.* **2016**, 1, 16013.
- [6] Y. Sun, N. Liu, Y. Cui, *Nat. Energy* **2016**, 1, 16071.
- [7] A. Manthiram, X. Yu, S. Wang, *Nat. Rev. Mater.* **2017**, 2, 16103.
- [8] K. Xi, B. Chen, H. Li, R. Xie, C. Gao, C. Zhang, R. V. Kumar, J. Robertson, *Nano Energy* **2015**, 12, 538.
- [9] J.-Y. Hwang, S.-T. Myung, Y.-K. Sun, *Adv. Funct. Mater.* **2018**, 28, 1802938.
- [10] J. Y. Hwang, S. T. Myung, Y. K. Sun, *Chem. Soc. Rev.* **2017**, 46, 3529.
- [11] Y. Huang, L. Zhao, L. Li, M. Xie, F. Wu, R. Chen, *Adv. Mater.* **2019**, 23, 1808393.
- [12] J. Xu, Y. Dou, Z. Wei, J. Ma, Y. Deng, Y. Li, H. Liu, S. Dou, *Adv. Sci.* **2017**, 4, 1700146.
- [13] L. Li, W. Zhang, X. Wang, S. Zhang, Y. Liu, M. Li, G. Zhu, Y. Zheng, Q. Zhang, T. Zhou, W. K. Pang, W. Luo, Z. Guo, J. Yang, *ACS Nano* **2019**, 13, 7939.
- [14] J. Zhou, Y. Liu, S. Zhang, T. Zhou, Z. Guo, *InfoMat* **2020**, 2, 437.
- [15] W. Zhang, Y. Liu, Z. Guo, *Sci. Adv.* **2019**, 5, eaav7412.
- [16] H. Kim, J. C. Kim, M. Bianchini, D.-H. Seo, J. Rodriguez-Garcia, G. Ceder, *Adv. Energy Mater.* **2018**, 8, 1702384.
- [17] L. Yang, X. Li, Y. Ouyang, Q. Gao, L. Ouyang, R. Hu, J. Liu, M. Zhu, *ACS Appl. Mater. Interfaces* **2016**, 8, 19987.
- [18] S. Lu, T. Zhu, H. Wu, Y. Wang, J. Li, A. Abdelkader, K. Xi, W. Wang, Y. Li, S. Ding, *Nano Energy* **2019**, 59, 762.
- [19] Z. Zhao, Z. Hu, R. Jiao, Z. Tang, P. Dong, Y. Li, S. Li, H. Li, *Energy Storage Mater.* **2019**, 22, 228.
- [20] H. Lin, M. Li, X. Yang, D. Yu, Y. Zeng, C. Wang, G. Chen, F. Du, *Adv. Energy Mater.* **2019**, 9, 1900323.
- [21] W. Wang, P. Li, H. Zheng, Q. Liu, F. Lv, J. Wu, H. Wang, S. Guo, *Small* **2017**, 13, 1702228.
- [22] X. Xu, R. Zhao, B. Chen, L. Wu, C. Zou, W. Ai, H. Zhang, W. Huang, T. Yu, *Adv. Mater.* **2019**, 31, 1900526.
- [23] K. Xi, D. He, C. Harris, Y. Wang, C. Lai, H. Li, P. R. Coxon, S. Ding, C. Wang, R. V. Kumar, *Adv. Sci.* **2019**, 6, 1800815.
- [24] J. Chu, Q. Yu, D. Yang, L. Xing, C.-Y. Lao, M. Wang, K. Han, Z. Liu, L. Zhang, W. Du, *Appl. Mater. Today* **2018**, 13, 344.
- [25] S. Lu, H. Wu, J. Hou, L. Liu, J. Li, C. J. Harris, C.-Y. Lao, Y. Guo, K. Xi, S. Ding, G. Gao, A. K. Cheetham, R. V. Kumar, *Nano Res.* **2020**, 13, 2289.
- [26] Q. Wang, W. Zhang, C. Guo, Y. Liu, C. Wang, Z. Guo, *Adv. Funct. Mater.* **2017**, 27, 1703390.
- [27] F. Yang, H. Gao, J. Hao, S. Zhang, P. Li, Y. Liu, J. Chen, Z. Guo, *Adv. Funct. Mater.* **2019**, 29, 1808291.
- [28] W. Li, B. Yan, H. Fan, C. Zhang, H. Xu, X. Cheng, Z. Li, G. Jia, S. An, X. Qiu, *ACS Appl. Mater. Interfaces* **2019**, 11, 22364.
- [29] Q. Liang, Y. Zheng, C. Du, Y. Luo, J. Zhang, B. Li, Y. Zong, Q. Yan, *Small Methods* **2017**, 1, 1700304.
- [30] X. Wang, K. Chen, G. Wang, X. Liu, H. Wang, *ACS Nano* **2017**, 11, 11602.
- [31] C. Wu, P. Kopold, P. A. van Aken, J. Maier, Y. Yu, *Adv. Mater.* **2017**, 29, 1604015.
- [32] W. Zhang, W. K. Pang, V. Sencadas, Z. Guo, *Joule* **2018**, 2, 1534.
- [33] W. Zhang, J. Mao, S. Li, Z. Chen, Z. Guo, *J. Am. Chem. Soc.* **2017**, 139, 3316.
- [34] Z. Li, Y. Fang, J. Zhang, X. W. D. Lou, *Adv. Mater.* **2018**, 30, 1800525.
- [35] L. Zhu, Z. Chen, Y. Song, P. Wang, Y. Jiang, L. Jiang, Y.-N. Zhou, L. Hu, *Nanoscale* **2018**, 10, 5581.
- [36] S. Zheng, X. Li, B. Yan, Q. Hu, Y. Xu, X. Xiao, H. Xue, H. Pang, *Adv. Energy Mater.* **2017**, 7, 1602733.
- [37] J. Deng, W. Luo, S. Chou, H. Liu, S. Dou, *Adv. Energy Mater.* **2018**, 8, 1701428.
- [38] L. Ma, S. Chen, Z. Pei, H. Li, Z. Wang, Z. Liu, Z. Tang, J. A. Zapien, C. Zhi, *ACS Nano* **2018**, 12, 8597.
- [39] F. Xie, L. Zhang, C. Ye, M. Jaroniec, S. Z. Qiao, *Adv. Mater.* **2018**, 31, 1800492.
- [40] M. Lao, Y. Zhang, W. Luo, Q. Yan, W. Sun, S. X. Dou, *Adv. Mater.* **2017**, 29, 1700622.
- [41] W. Wang, B. Jiang, C. Qian, F. Lv, J. Feng, J. Zhou, K. Wang, C. Yang, Y. Yang, S. Guo, *Adv. Mater.* **2018**, 30, 1801812.
- [42] M. Chen, Y. Zhang, L. Xing, Y. Liao, Y. Qiu, S. Yang, W. Li, *Adv. Mater.* **2017**, 29, 1607015.
- [43] Q. Li, Q. Wei, Q. An, L. Huang, W. Luo, X. Ren, K. A. Owusu, F. Dong, L. Li, P. Zhou, *Energy Storage Mater.* **2019**, 16, 625.
- [44] X. Min, B. Sun, S. Chen, M. Fang, X. Wu, Y. g. Liu, A. Abdelkader, Z. Huang, T. Liu, K. Xi, *Energy Storage Mater.* **2019**, 16, 597.
- [45] Z. Liu, T. Lu, T. Song, X.-Y. Yu, X. W. Lou, U. Paik, *Energy Environ. Sci.* **2017**, 10, 1576.
- [46] Y. Li, K. Yan, H.-W. Lee, Z. Lu, N. Liu, Y. Cui, *Nat. Energy* **2016**, 1, 15029.
- [47] P. Ge, H. Hou, S. Li, L. Yang, X. Ji, *Adv. Funct. Mater.* **2018**, 28, 1801765.
- [48] C. An, Y. Yuan, B. Zhang, L. Tang, B. Xiao, Z. He, J. Zheng, J. Lu, *Adv. Energy Mater.* **2019**, 23, 1900356.
- [49] J. H. Choi, S. K. Park, Y. C. Kang, *Small* **2019**, 15, 1803043.
- [50] Y. Tang, Z. Zhao, X. Hao, Y. Wei, H. Zhang, Y. Dong, Y. Wang, X. Pan, Y. Hou, X. Wang, J. Qiu, *J. Mater. Chem. A* **2019**, 7, 4469.
- [51] Z. Zhang, X. Shi, X. Yang, Y. Fu, K. Zhang, Y. Lai, J. Li, *ACS Appl. Mater. Interfaces* **2016**, 8, 13849.
- [52] M. Shenasa, S. Sainkar, D. Lichtman, *J. Electron Spectrosc. Relat. Phenom.* **1986**, 40, 329.
- [53] H. Wang, X. Wang, Q. Li, H. Li, J. Xu, X. Li, H. Zhao, Y. Tang, G. Zhao, H. Li, H. Zhao, S. Li, *ACS Appl. Mater. Interfaces* **2018**, 10, 38862.
- [54] J. Wang, F. Kong, J. Chen, Z. Han, S. Tao, B. Qian, X. Jiang, *ChemElectroChem* **2019**, 6, 2805.
- [55] K. Zhang, Z. Hu, X. Liu, Z. Tao, J. Chen, *Adv. Mater.* **2015**, 27, 3305.
- [56] H.-L. Girard, H. Wang, A. d'Entremont, L. Pilon, *J. Phys. Chem. C* **2015**, 119, 11349.
- [57] S. Lu, T. Zhu, Z. Li, Y. Pang, L. Shi, S. Ding, G. Gao, *J. Mater. Chem. A* **2018**, 6, 7005.
- [58] S. Lu, Y. Gao, Z. Li, B. Dong, T. Gao, S. Ding, Y. Bai, G. Gao, *J. Alloys Compd.* **2018**, 749, 424.
- [59] D. Li, Q. Sun, Y. Zhang, L. Chen, Z. Wang, Z. Liang, P. Si, L. Ci, *ChemSusChem* **2019**, 12, 2689.
- [60] J. Ge, L. Fan, J. Wang, Q. Zhang, Z. Liu, E. Zhang, Q. Liu, X. Yu, B. Lu, *Adv. Energy Mater.* **2018**, 8, 1801477.
- [61] S. Zhang, G. Wang, J. Jin, L. Zhang, Z. Wen, J. Yang, *ACS Nano* **2018**, 12, 4010.
- [62] H. Tian, X. Yu, H. Shao, L. Dong, Y. Chen, X. Fang, C. Wang, W. Han, G. Wang, *Adv. Energy Mater.* **2019**, 9, 1901560.